Volume 1 | Number 1 | Jan 2013 | Pages 1–100

Nanoscale

www.rsc.org/nanoscale

ROYAL SOCIETY
OF CHEMISTRY

ROYAL SOCIETY
OF CHEMISTRY

www.rsc.org/nanoscale

Journal Name

COMMUNICATION

How to choose a precursor for decomposition solution-phase synthesis: The case of iron nanoparticles

David A. J. Herman[a], Soshan Cheong[a], Andrew J. McGrath[a], Benjamin F. P. McVey[a], Matthias Lein[a], Richard D. Tilley*[a]

The decomposition of organometallic compounds as precursors has revolutionized the synthesis of nanoparticles in solution. However, effective control of size and size distribution of iron nanoparticles has remained challenging due to the high reactivity of iron towards oxygen or oxygen-containing materials. Reported is a decomposition study that shows how metal to ligand bonding and symmetry of the compound can be manipulated to control the size and size distribution of iron nanoparticles in the 6-16 nm range. $[Fe(\eta^5-C_6H_3Me_4)_2]$ was found to be the optimal precursor with a narrow decomposition temperature range due to its symmetry and the low bond dissociation energy of the ligands from the Fe(II) center. The precise control of nanoparticle size has enabled the tuning of magnetic properties from superparamagnetic to soft-ferromagnetic desirable for a wide range of biomedical applications.

Controlling the size and shape of nanoparticles enables the control of their properties.[1] In solution-phase synthesis, size monodispersity can be achieved by optimizing the decomposition of the metal precursor to control the growth of the nanoparticles.[2,3] Organometallic compounds are suitable precursors for use in the synthesis of nanoparticles due to their reactivity and solubility, and have been used to synthesize semiconductor, catalytic and magnetic nanoparticles.[4]

Magnetic nanoparticles are widely researched due to their bio-applications such as magnetic resonance imaging (MRI), drug delivery and magnetic hyperthermia.[5] Iron nanoparticles are ideal candidates for these applications due to their high magnetization and biocompatibility.[6] For successful bio-application, the iron nanoparticles need to be 16 nm or smaller in size to display either a soft-ferromagnetic or superparamagnetic behavior.[7] Iron nanoparticles larger than 16 nm are ferromagnetic and irreversibly aggregate in the body during MRI or hyperthermia.[8] Initial studies for the synthesis of iron nanoparticles were achieved by the decomposition of iron pentacarbonyl, $[Fe(CO)_5]$.[9] Other precursors, namely iron bis(trimethylsilyl)amide, $Fe[N(Si(CH_3)_3)_2]$, and iron oleate have been used to synthesize iron nanocubes.[10] However, ease of synthesis is limited; $[Fe(CO)_5]$ is highly toxic and has a complex decomposition pathway[11], while other precursors are either air-

sensitive or require high reaction temperatures.[10] Therefore obtaining stable iron nanoparticles with controlled size from suitable precursors and simple synthetic procedures has remained challenging.[11]

Here we describe the synthesis of iron nanoparticles using three iron sandwich compounds having different decomposition profiles controlled by the symmetry and metal-ligand bond dissociation energies of the compounds. We show how these properties alter the size and monodispersity of the iron nanoparticles. The precursors investigated were i) bis(1,3,5-*exo*-6-tetramethyl-η^5-cyclohexadienyl)iron, $[Fe(\eta^5-C_6H_3Me_4)_2]$, ii) ($\eta^5$-cyclopentadienyl)($\eta^5$-cyclohexadienyl)iron, $[Fe(\eta^5-C_5H_5)(\eta^5-C_6H_7)]$ and iii) ferrocene or bis(η^5-cyclopentadienyl)iron, $[Fe(\eta^5-C_5H_5)_2]$. The iron precursors were thermally decomposed in a mixture of oleylamine as a capping agent and 1-octadecene as the solvent at 300 °C, at which the reaction mixture was maintained for 2 hours. Upon cooling to room temperature, products were isolated by means of magnetic separation.

Fig. 1a shows a transmission electron microscopy (TEM) image of the spherical, core/shell nanoparticles obtained from the decomposition of $[Fe(\eta^5-C_6H_3Me_4)_2]$ with a yield of 71% (see Fig. 1a inset for compound structure). The nanoparticles are relatively monodisperse with an average size of 15.8 ± 1.6 nm. The contrast of the nanoparticles in the image shows darker cores surrounded by lighter contrast shells revealing heterogeneous core/shell structures. The average core size and shell thickness were measured to be ~11 and ~2.5 nm, respectively (Fig. S1). High-resolution TEM (HRTEM) analysis and selected area electron diffraction (SAED) confirm the presence of a single crystal, body-centered cubic α-Fe core and a polycrystalline spinel iron oxide shell with multiple domains (Figs. S2 and S3a). Fig. 1b shows the nanoparticles obtained when the precursor was replaced with the asymmetrical $[Fe(\eta^5-C_5H_5)(\eta^5-C_6H_7)]$ compound (see Fig. 1b inset for compound structure). The nanoparticles are irregular in shape with nanoparticle size varies between 3 and 22 nm. The sample consists of both iron/iron oxide core/shell nanoparticles and small iron oxide nanoparticles (Fig. S3b). Fig. 1c shows the nanoparticles obtained from decomposing $[Fe(\eta^5-C_5H_5)_2]$, which has a D_{5d} symmetry (see Fig. 1c inset for compound structure). The nanoparticles are highly irregular iron/iron oxide core/shell structures, with a relatively broad size range of 10-60 nm

(Fig. S3c). The color of the reaction mixture remained yellow with ~1 mg of core/shell nanoparticles collected (~2% yield), due to the stability of the precursor leading to incomplete precursor decomposition. Fig. 1d shows the powder X-ray diffraction (XRD) pattern of the nanoparticles synthesized from [Fe(η^5-C$_6$H$_3$Me$_4$)$_2$], indexed to α-Fe and iron oxide (*) of either Fe$_3$O$_4$ or γ-Fe$_2$O$_3$ phase.[12] An IR spectra of the nanoparticles shown in Fig 1a is shown in Fig. S4 and indicates that the nanoparticles are oleylamine coated.
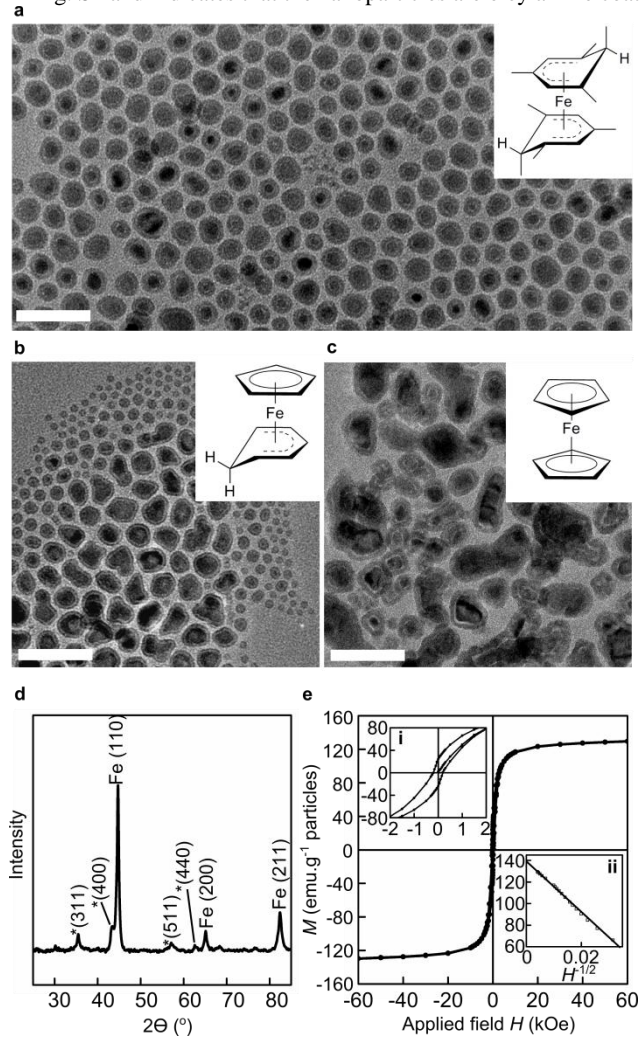

Fig. 1 TEM images of iron/iron oxide core/shell nanoparticles made from the decomposition of (a) [Fe(η^5-C$_6$H$_3$Me$_4$)$_2$], (b) [Fe(η^5-C$_5$H$_5$)(η^5-C$_6$H$_7$)] and (c) [Fe(η^5-C$_5$H$_5$)$_2$], with insets showing the respective precursor structures. The scale bars are 50 nm. (d) Powder XRD pattern of nanoparticles as shown in (a), with diffraction peaks indexed to α-Fe and spinel iron oxide phase (*). (e) Magnetic hysteresis at 300 K of the nanoparticles in (a); insets show (i) low field regions and (ii) plot of magnetization (M) against $H^{-1/2}$ (where H is the applied field), fitted with a linear function shown by the solid line.

The magnetic hysteresis loop of the core/shell nanoparticles synthesized from [Fe(η^5-C$_6$H$_3$Me$_4$)$_2$] is shown in Fig. 1e. As seen in inset (i), the nanoparticles exhibit a soft-ferromagnetic behavior, with a remnant magnetization of ~24 emu.g^{-1}, and a coercivity of ~200 Oe. Inset ii shows the sample approached saturation according to the relationship $M \propto H^{-1/2}$, with M being the magnetization and H the applied field, and the saturation magnetization (M_S) was determined

to be 139 emu.g^{-1}. This magnetization is in agreement with previous reports of iron/iron oxide core/shell nanoparticles with similar sizes[10].
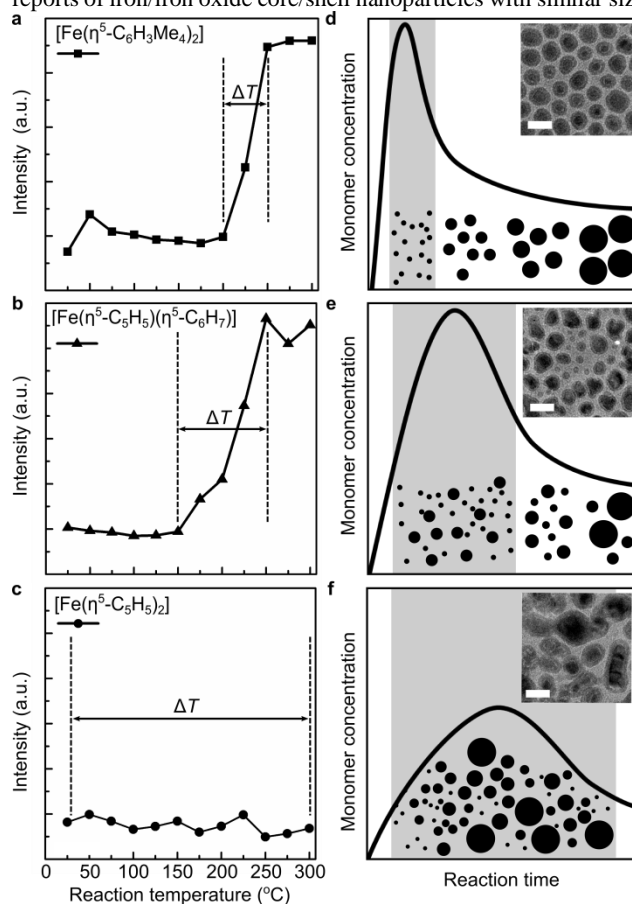

Fig. 2 Plots showing how the intensity of UV-vis absorption changes at (a) 462, (b) 413 and (c) 441 nm for compounds [Fe(η^5-C$_6$H$_3$Me$_4$)$_2$], [Fe(η^5-C$_5$H$_5$)(η^5-C$_6$H$_7$)] and [Fe(η^5-C$_5$H$_5$)$_2$] respectively, with the increase of reaction temperature. ΔT indicates the respective decomposition temperature range for each compound. (e-f) Schematic illustrations of LaMer models correspond to the decompositions observed in (a-c), respectively, with insets showing TEM images of the nanoparticles obtained from the different precursors. The scale bars are 20 nm in (e-f).

To investigate the effect precursor structure had on the iron nanoparticles' size, UV-vis spectroscopy experiments were performed to monitor nanoparticle synthesis.[13] The formation of nanoparticles was accompanied by a color change from yellow-orange to brown, which allowed for absorption intensity at selected wavelengths to be monitored and the decomposition temperature range (ΔT) determined. Fig. 2a plots the absorbance at 462 nm of [Fe(η^5-C$_6$H$_3$Me$_4$)$_2$] being heated from room temperature to 300 °C. (See Fig. S5 for UV-vis spectra and details of the analysis.) The peak intensity remains relatively constant until ~200 °C, where a significant increase in intensity can be observed between 200-250 °C, with a ΔT of ~50°C (between 200-250 °C), indicating a rapid formation of nanoparticles. Fig. 2b plots the absorbance at 348 nm of [Fe(η^5-C$_5$H$_5$)(η^5-C$_6$H$_7$)], where a ΔT of ~100°C is observed (between 150-250°C) indicating a slower decomposition. Fig. 2c plots the absorbance at 441 nm of [Fe(η^5-C$_5$H$_5$)$_2$], where no significant change in the intensity can be observed, indicating limited precursor decomposition and nanoparticle formation.
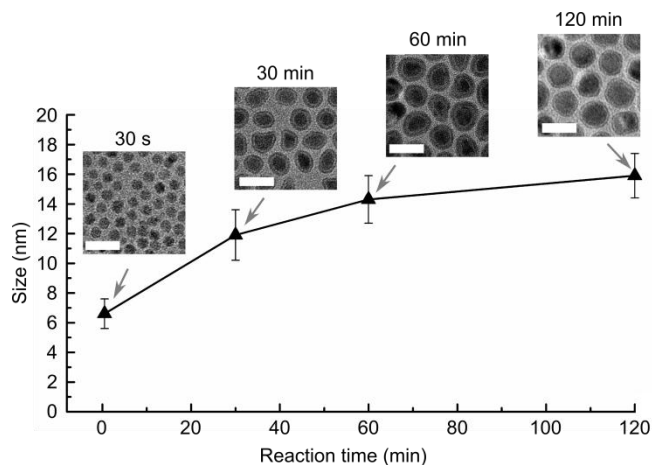
Fig. 3 Plot of nanoparticle size against reaction time for nanoparticles obtained at 30 s, 30, 60 and 120 min from the decomposition of $[Fe(\eta^5\text{-}C_6H_3Me_4)_2]$, and the corresponding TEM images. Standard deviations are shown as error bars. The scale bars are 20 nm.

The difference in the size distribution of the iron nanoparticles obtained by altering the precursor structure can be attributed to differences in the nucleation stage when the nanoparticles form, as explained by the LaMer model.[14] The narrow ΔT of $[Fe(\eta^5\text{-}C_6H_3Me_4)_2]$ results in a rapid nucleation event followed by separate uniform growth to form monodisperse iron nanoparticles with average size of 15.8 ± 1.6 nm, which can be illustrated using a LaMer plot in Fig. 2d. The larger decomposition ΔT for $[Fe(\eta^5\text{-}C_5H_5)(\eta^5\text{-}C_6H_7)]$ results in a broad nucleation and simultaneous growth, resulting in an increased size range of 3-22 nm of the nanoparticles, as illustrated in Fig. 2e.[15] The decomposition of $[Fe(\eta^5\text{-}C_5H_5)_2]$ leads to only a minimal amount of precursor reacting, resulting in irregular, polydisperse nanoparticles with a relatively large size range of 10-60 nm, as illustrated in the LaMer plot shown in Fig. 2f.[15]

To understand the difference in the precursor decomposition temperature range, computational calculations on the bond dissociation energies (BDEs) of the ligand(s) from each precursor's Fe(II) center were performed (Table S1). For $[Fe(\eta^5\text{-}C_6H_3Me_4)_2]$ and $[Fe(\eta^5\text{-}C_5H_5)_2]$, the BDE of the ligands were -199.4 and -224.6 kJ.mol^{-1}, respectively. This difference is due to the presence of the cyclopentadienyl rings, $(C_5H_5)-$, which require more thermal energy to liberate the Fe(II) because cyclopentadienyl rings have strong affinity for Fe(II) centres.[16] For $[Fe(\eta^5\text{-}C_5H_5)(\eta^5\text{-}C_6H_7)]$, two BDEs are calculated, -209.4 and -233.5 kJ.mol^{-1} for the dissociation of $(\eta^5\text{-}C_5H_5)-$ and $(\eta^5\text{-}C_6H_7)-$, respectively. The different BDEs indicate that only partial dissociation occurs of $[Fe(\eta^5\text{-}C_5H_5)(\eta^5\text{-}C_6H_7)]$ upon decomposition at 300°C, broadening the decomposition ΔT and the nucleation event observed in Fig. 2b.

The size of the iron nanoparticles synthesized from $[Fe(\eta^5\text{-}C_6H_3Me_4)_2]$ can be controlled and tuned by altering the reaction time. Fig. 3 shows the controlled increase in the nanoparticle size from 6 to 16 nm with increasing reaction time from 30 s to 120 min with the decomposition of $[Fe(\eta^5\text{-}C_6H_3Me_4)_2]$ at 300°C. After 30 s, the nanoparticles are 6.6 ± 1.1 nm in size which has fully oxidized on exposure to air to form iron oxide nanoparticles. Iron nanoparticles smaller than 8 nm have been reported to fully oxidize upon exposure to air.[17] Further increasing the reaction time to 30 min resulted in an increase in nanoparticle size to 11.9 ± 1.7 nm with an iron core size of ~ 8 nm and iron oxide shell thickness of ~ 2.5 nm (Fig. S6). After 120 min the iron nanoparticles reach a final size of ~16 nm, with α-Fe core averages at ~11 nm and oxide shell thickness remains at ~2.5 nm.

With nanoparticle size precisely controlled, the magnetic properties of the iron nanoparticles could be tuned from superparamagnetic to soft-ferromagnetic by increasing reaction time from 30 s to 120 min. After 30 s, the 6 nm iron oxide nanoparticles have no remnant magnetization or coercivity indicating the nanoparticles are superparamagnetic, with a M_S of 42 emu.g^{-1} (Fig. S7). When the reaction time is increased to 120 min, the 16 nm iron nanoparticles become soft-ferromagnetic with a M_S of 139 emu.g^{-1}, as shown in Fig. 1e. Such tuning of magnetic properties is desired to achieve optimal contrast enhancement in MRI and to prevent irreversible aggregation.[18]

Conclusions

In summary, we showed that by altering the symmetry and bond dissociation energy of the organometallic precursor we can control the decomposition profile of different organometallic compounds to control the size and size distribution of nanoparticles. This was illustrated with iron metal where sandwich compounds containing different aromatic ligands gave monodisperse nanoparticles with sizes ranging from 6 to 16 nm. By controlling the size, the magnetic properties of the nanoparticles were also tuned from superparamagnetic to soft-ferromagnetic. The role of decomposition of the precursor in controlling size and monodispersity was investigated using UV-vis spectroscopy and computational calculations. The results show the importance of choosing organometallic compounds with the optimal symmetry and metal-ligand bond dissociation energies to give a narrow decomposition ΔT to produce monodispersed nanoparticles.

Notes and references

^{a} School of Chemical and Physical Sciences and the MacDiarmid Institute for Advanced Materials and Nanotechnology, Victoria University of Wellington, P.O. Box 600, Wellington 6140, New Zealand.

† Electronic Supplementary Information (ESI) available: Experimental details and additional characterization data. See DOI: 10.1039/c000000x/

1   (a) Y. Yin and A. P. Alivisatos, *Nature*, 2005, **437**, 664-670; (b) A. M. Henning, J. Watt, P. J. Miedziak, S. Cheong, M. Santonastaso, M. Song, Y. Takeda, A. I. Kirkland, S. H. Taylor and R. D. Tilley, *Angew. Chem. Int. Ed.*, 2013, **52**, 1477-1480.

2   J. Park, J. Joo, S. G. Kwon, Y. Jang and T. Hyeon, *Angew. Chem. Int. Ed.*, 2007, **46**, 4630-4660.

3   C. B. Murray, D. J. Norris and M. G. Bawendi, *J. Am. Chem. Soc.*, 1993. **115**, 8706-8715.

4   (a) B. Chaudret, *C. R. Phys.*, 2005, **6**, 117-131; (b) M. Green, *Chem. Commun.*, 2005, 3002-3011.

5   (a) D. Yoo, J.-H. Lee, T.-H. Shin and J. Cheon, *Acc. Chem. Res.*, 2011, **44**, 863-874; (b) R. Weissleder, M. Nahrendorf and M. J. Pittet, *Nat Mater.*, 2014, **13**, 125-138; (c) E.-K. Lim, T. Kim, S. Paik, S. Haam, Y.-M. Huh and K. Lee., *Chem. Rev.* 2015. **115**, 327-394.

6   S. Cheong, P. Ferguson, K. W. Feindel, I. F. Hermans, P. T. Callaghan, C. Meyer, A. Slocombe, C.-H. Su, F.-Y. Cheng, C.-S. Yeh, B. Ingham,

Nanoscale Accepted Manuscript

M. F. Toney and R. D. Tilley, *Angew. Chem. Int. Ed.*, 2011, **50**, 4206-4209.

7   A. H. Lu, E. L. Salabas and F. Schuth, *Angew. Chem. Int. Ed.*, 2007, **46**, 1222-1244.

8   H. B. Na, I. C. Song and T. Hyeon, *Adv. Mater.*, 2009, **21**, 2133-2148.

9   (a) L.-M. Lacroix, N. Frey Huls, D. Ho, X. Sun, K. Cheng and S. Sun, *Nano Lett.*, 2011, **11**, 1641-1645; (b) A. Meffre, B. Mehdaoui, V. Kelsen, P. F. Fazzini, J. Carrey, S. Lachaize, M. Respaud and B. Chaudret, *Nano Lett.*, 2012, **12**, 4722-4728; (c) T. C. Monson, Q. Ma, T. E. Stevens, J. M. Lavin, J. L. Leger, P. V. Klimov and D. L. Huber, *Part. Part. Syst. Charact.*, 2013, **30**, 258-265.

10 (a) F. Dumestre, B. Chaudret, C. Amiens, P. Renaud and P. Fejes, *Science*, 2004, **303**, 821-823; (b) A. Shavel, B. Rodriguez-Gonzalez, M. Spasova, M. Farle and L. M. Liz-Marzan, *Adv. Funct. Mater.*, 2007, **17**, 3870-3876; (c) D. Kim, J. Park, K. An, N.-K. Yang, J.-G Park and T. Hyeon, *J. Am. Chem. Soc.*, 2007, **129**, 5812-5813.

11 D. L. Huber. *Small*, 2005, **1**, 482-501.

12 J. H. L. Beal, S. Prabakar, N. Gaston, G. B. Teh, P. G. Etchegoin, G. Williams and R. D. Tilley, *Chem. Mater.*, 2011, **23**, 2514-2517.

13 M. F. Casula, Y.-W. Jun, D. J. Zaziski, E. M. Chan, A. Corrias and A. P. Alivisatos, *J. Am. Chem. Soc.*, 2006, **128**, 1675-1682.

14 V. K. LaMer and R. H. Dinegar, *J. Am. Chem. Soc.*, 1950, **72**, 4847-4854.

15 C. D. Donega, P. Liljeroth and D. Vanmaekelbergh, *Small*, 2005, **1**, 1152-1162.

16 K. E. Lewis and G. P. Smith, *J. Am. Chem. Soc.*, 1984, **106**, 4650-4651.

17 S. Peng, C. Wang, J. Xie and S. H. Sun, *J. Am. Chem. Soc.*, 2006, **128**, 10676-10677.

18 D. Ho, X. Sun and S. Sun, *Acc. Chem. Res.*, 2011, **44**, 875-882.

Nanoscale Accepted Manuscript